ARTICLE IN PRESS

Journal of the European Ceramic Society xxx (xxxx) xxx

Contents lists available at ScienceDirect

Journal of the European Ceramic Society

journal homepage: www.elsevier.com/locate/jeurceramsoc

Original Article

Mechanical properties of 3D printed ceramic cellular materials with triply periodic minimal surface architectures

Minhao Shen [a,1], Wei Qin [b,1], Bohang Xing [a], Weiming Zhao [a], Shuyue Gao [a], Ying Sun [a], Ting Jiao [b,*], Zhe Zhao [a,*]

[a] School of Material Science and Engineering, Shanghai Institute of Technology, Shanghai, 201418, China
[b] Department of Prosthodontics, Shanghai Ninth People's Hospital, College of Stomatology, Shanghai Jiao Tong University School of Medicine, Shanghai, 200011, China

ARTICLE INFO

Keywords:
Ceramics
DLP
Triply periodic minimal surfaces
Young's modulus

ABSTRACT

In this study, four types of triply periodic minimal surface (TPMS) were implemented to create cellular ceramics via digital light processing (DLP) technology, namely p-cell, gyroid, IWP and s14. The mechanical properties of these TPMS structures were investigated experimentally. Results showed that compressive strength of TPMS structures increases with relative density. IWP and s14 structures exhibit similar mechanical response under stress. In general, all TPMS structures can sustain >2% strain without failure and the compressive strength followed the order of s14 > IWP > gyroid > p-cell. The s14 structure can reach a high compressive strength of 105 MPa at a structural density of 30.5 % while gyroid structure can provide a compressive strength of 5.6 MPa at a very low structural density of 6.7 %. The porosity dependence of Young's modulus of sintered zirconia TPMS demonstrated that the Pabst-Gregorova exponential relation can provide a better prediction than the classical Gibson-Ashby model.

1. Introduction

Cellular materials are a class of materials that are characterized by low density and high specific properties. These properties include acoustic [1], electrical [2] and thermal [3] and mechanical properties [4]. Several researchers have used experimental, computational, and analytical approaches to study the linear and nonlinear mechanical [5] responses of cellular materials, including elastic properties [6], yielding, buckling, and effects of imperfections. These studies revealed that the properties of the base material, the lattice structure and the relative density of the structure all affect overall performance. When the base material and relative density of the model are fixed, the mechanical properties of the cellular structure are mainly determined by the geometric characteristics of the unit cell.

Research interest in cellular materials has recently shifted to cellular structures with mathematically defined architectures such as triply periodic minimal surfaces (TPMSs). The TPMS structures possess a zero mean curvature. They are complex 3D topologies that locally minimize surface area for a given boundary condition and can be repeated periodically in three perpendicular directions [7–11]. Unfortunately, the difficulties of crafting these complex TPMS structures with reasonable geometric precision by traditional forming methods has been an obstacle for quite a long time [12,13]. With the development of 3D printing technology, the accurate preparation of TPMS structures has become more feasible.

Recently, several studies on cellular solids with TPMS structures made of polymers [14–16] and metals [4,17–19] have been reported. Abueidda et al. [14,15] studied the differences between the mechanical properties of various TPMS structures, Maskery et al. [16] studied the deformation mechanism of TPMS structure by combining the experiment and Gibson-Ashby model [20] theory. Metallic TPMS cellular structures have been studied, and interesting results have been reported in the literature. Different from polymer TPMS, Ketan et al. [17] made some changes to the structure of metallic TPMS by CAD, establishing sheet-based or skeletal-based structures, and evaluated their mechanical properties. Similarly, they also used the GA model to evaluate the deformation mechanism of metal TPMS structures.

However, regardless of the TPMS structure prepared by polymers or metal materials, researchers have focused on the exponent of the Gibson-Ashby (GA) model [20] (the n value of the power law function),

* Corresponding authors.
E-mail addresses: jiao_ting@126.com (T. Jiao), zhezhao@sit.edu.cn (Z. Zhao).
[1] These authors contributed equally to this work and should be considered co-first authors.

https://doi.org/10.1016/j.jeurceramsoc.2020.09.062
Received 5 August 2020; Received in revised form 25 September 2020; Accepted 26 September 2020
Available online 29 September 2020
0955-2219/© 2020 Elsevier Ltd. All rights reserved.

Table 1
Sintering conditions.

Step	Temperature/°C	Time/min	Temperature rate/°C min^{-1}
1	0–200	40	5
2	200–600	400	1
3	600–1550	190	5
4	1550	120	0

and more or less ignored the discussion of applicability of the GA model. It is essential to build up the constitutive model for these interesting lightweight/lattice structures if they want to be implemented for real engineering projects. Recently, ceramic TPMS structures [21–23] was successfully achieved by novel 3D printing technology, but the effort of a full understanding of the porosity dependence of mechanical properties is still missing. Experience shows that for periodic open-cell structures the effective property values predicted by the GA model are usually higher than the experimental data, which is usually attributed to microstructural defects. This argumentation, however, is disputable. Pabst et al. [24] derived the Pabst-Gregorová (PG) exponential relation on the basis of a so-called functional equation approach. This function provided a better agreement between experimental data and the numerical calculations [25,26], which seems to be a more accurate prediction than the GA model for the effective performance of periodic lattice structures. Actually, there are few reports on the prediction of effective properties of 3D printed ceramic TPMS structures by the GA model or the PG exponential relation.

In this paper, we used zirconia as the raw material to prepare four different TPMS structures via the DLP technique. In this case, we systematically modified the cell numbers and cell size, thus we obtained the mechanical properties for various TPMS structures with a wide range of porosities. Here, mechanical properties, including the compressive strength, elastic modulus and energy absorption were carefully examined. Finally, based on the experimental data, we discuss the applicability of the GA model and the PG exponential relation for the porosity dependence of Young's modulus.

2. Experimental procedure

2.1. Material fabrication

The ZrO_2 mixed photopolymer resin and the printer are both provided by Jiaxing CeramPlus Co. Ltd. The printer has a layer thickness of 50 μm, and the minimum projected spot area of the printer is 50 μm × 50 μm. Four different structures—p-cell, gyroid, IWP, and s14—were fabricated. After the printing process, they were sintered to 1550 °C in a muffle furnace (KF1700, Nanjing Boyuntong Instrument Technology Co., Ltd., China). All specimens were sintered immediately after fabrication to eliminate possible changes in the mechanical properties of the ceramics. Table 1 outlines the sintering conditions.

2.2. Specimens

In the current work, TPMS structures are used to create architecture cellular materials. The methodology adopted to create the computer-aided design (CAD) files of these structures is similar to that reported in [2].

The shape of all the TPMS samples was retained as a cube with an edge length of 10 mm. For the convenience of printing and mechanical property testing, plates with a geometry of 10 mm × 10 mm × 0.3 mm were added to the top and bottom of the samples. There was no plate on the gyroid due to its special structure. To produce different relative densities, the shell thickness was designed to be 0.1 mm, and the unit cell of the samples was varied. The unit cell size was changed from 2 to 5 mm, and thus, we generated TPMS lattices denoted as 2 × 2×2, 3 × 3×3, 4 × 4×4 and 5 × 5×5. In Figs. 1 and 2, schematic diagrams of the TMPS unit cells and the printed-and-sintered ceramic TPMS samples are presented.

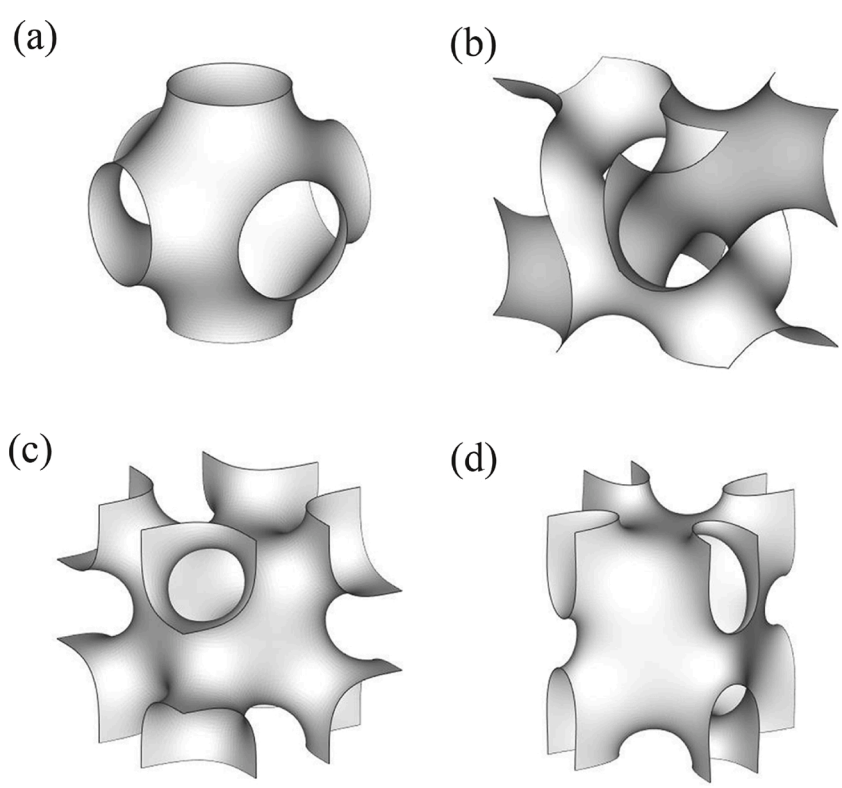

Fig. 1. Four different TPMS structure models.
(a) p-cell; (b) gyroid; (c) IWP; (d) s14

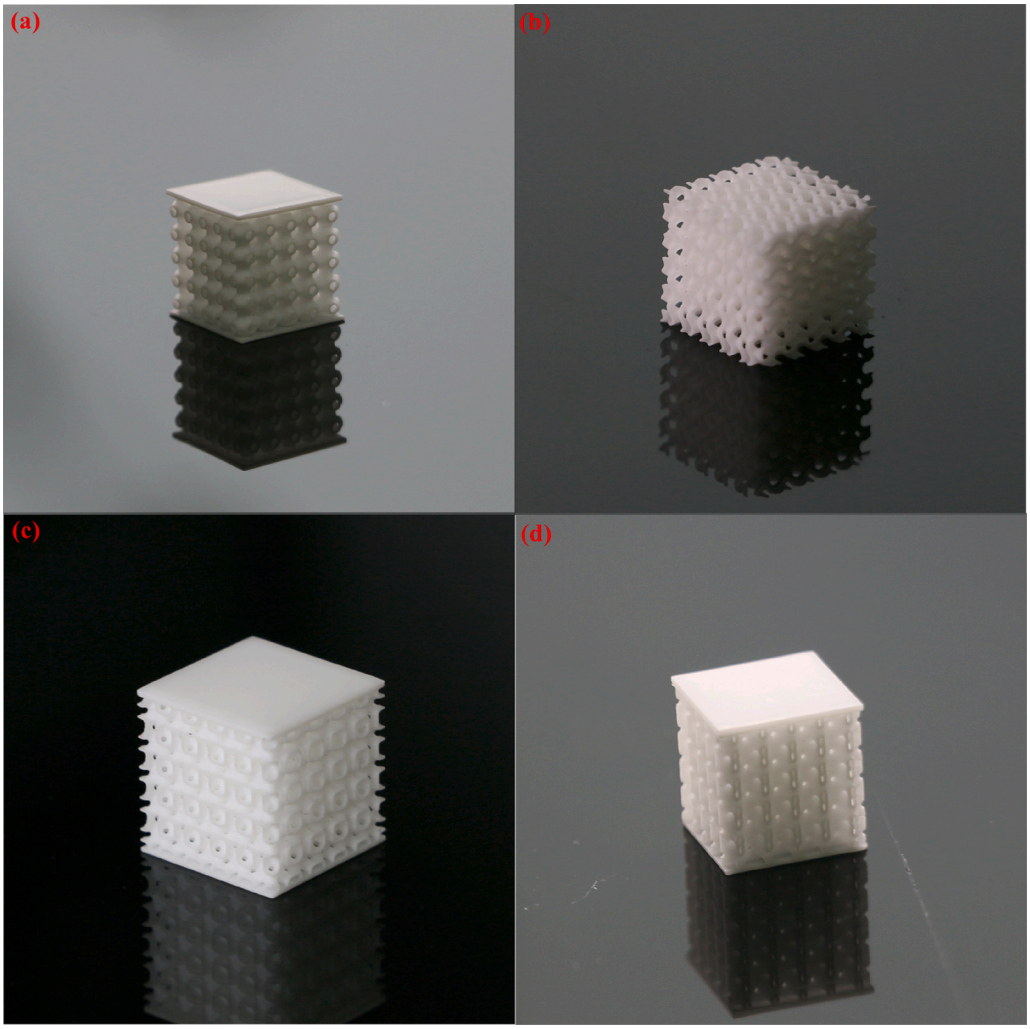

Fig. 2. Four samples of TPMS structures.
(a) 5 × 5×5 p-cells; (b) 5 × 5×5 gyroid cells;
(c) 5 × 5×5 IWP cells; (d) 5 × 5×5 s14 cells

2.3. Mechanical testing

The mechanical behavior of ceramics is strongly dependent on the applied strain rate, material type, and sintering schedule. In this work, we only applied mechanical load in the DLP building direction. The compressive loading rate was 0.2 mm/min. This can be considered a quasi-static experiment. In the case of compression loading, the specimens were tested until their collapse. For each compression test result, >5 samples were always tested. Force and displacement output were obtained from Universal testing machine (SUN500, Cardanoal Camp, Italy). Stress σ and strain ε were calculated using the equations below.

$$\sigma = \frac{F}{A_c} \tag{1}$$

$$\varepsilon = \frac{D}{h} \tag{2}$$

where F is the applied load, A_c is the cross-sectional area of the structure, D is the total displacement and h is the original height of the structure. In this paper, the value of A_c is 100 mm^2 and the value of h is 10.6 mm. (h of gyroid structure is 10 mm).

3. Results and discussion

3.1. Characterization of material and structures

As seen in Fig. 3, the sintered zirconia ceramic possesses a dense and uniform microstructure with a grain size of approximately 1 μm. After sintering at 1550 °C, the density of the 3Y-TZP ceramic reached ≥ 6.01 g/cm^3, which is a relative density of approximately 99 %, if 6.07 g/cm^3 is taken as the theoretical density. Actually, the translucency exhibited by the sintered TPMS structures (Fig. 2) also demonstrated that the porosity in all the samples was very limited. Principally, we can expect that the mechanical properties of the studied TPMS structures are affected by the microstructural defects. However, the obtained mechanical properties of bulk samples sintered under the same conditions can be regarded as the baseline for these ceramic TPMS structures.

Table 2 shows the comparison between the designed density and real density of four typical TPMS structures with different unit cells. Different from the reported results with metallic TPMS structures prepared by the SLM method [27], where the deviation in the relative density is surprisingly small, the real density is always much higher than the designed density for all the studied ceramic TPMS structures. In most cases, the real density is approximately twice the designed density, obviously because light is scattered during the printing process. However, there is no clear tendency for the deviation to be linked with the

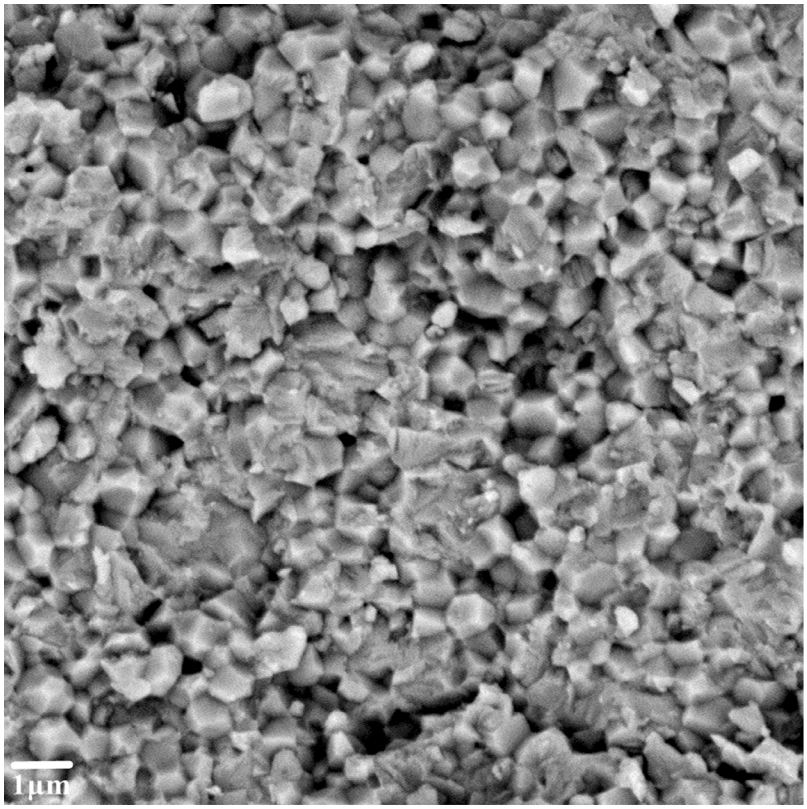

Fig. 3. SEM image of a fracture surface typical for all the structures.

Table 2
Designed density vs real density of the printed samples.

TPMS structures		2 × 2×2	3 × 3×3	4 × 4×4	5 × 5×5
P-cell	Designed density (a)	4.7 %	7.0 %	9.3 %	11.6 %
	Real density (b)	10.0 %	14.6 %	16.4 %	23.0 %
	b/a	2.15	2.09	1.76	1.98
Gyroid	Designed density (a)	6.0 %	9.0 %	11.9 %	14.9 %
	Real density (b)	6.7 %	16.8 %	20.9 %	27.6 %
	b/a	1.12	1.87	1.75	1.85
Iwp	Designed density (a)	6.9 %	10.3 %	13.7 %	17.0 %
	Real density (b)	14.0 %	20.6 %	27.8 %	33.6 %
	b/a	2.03	2.00	2.03	1.98
S14	Designed density (a)	6.0 %	8.9 %	11.9 %	14.7 %
	Real density (b)	12.9 %	19.6 %	21.8 %	30.5 %
	b/a	2.15	2.20	1.84	2.07

changed unit cell numbers.

To obtain a better understanding of the large deviation in ceramic DLP printing, we carefully examined the as-printed TPMS structures by SEM (see Fig. 4). Interestingly, in all four structures, the characteristic thickness of the shell was approximately 200 μm, although it was nominally kept at 100 μm in all the original designs. The doubled shell thickness in the as-printed TMPS structures indicated that light scattering is quite serious in the zirconia printing slurry. The overgrowth for a single free edge can be estimated to be approximately 50 μm. In contrast to the reported overgrowth behavior in [28], where the overgrowth was found to be affected by either the exposure intensity and time or side length, we found that this light-scattering-induced overgrowth only affected the absolute geometry size perpendicular to the free edge and did not change with the side length. Considering the high refraction index of ZrO_2 and the high solid load realized in this study (50 vol%), the light scattering-induced overgrowth reported here is rather low, which may indicate that the low viscosity and better particle dispersion might be the key reason for this excellent overgrowth control.

The DLP method was developed based on the DMD (Digital Micromirrors Device) chip, and the original shape of each projected pixel is a square with a size of 50 μm × 50 μm, so it is impossible for this method to realize a smooth path for any curved surface, and it is necessary to see if the obtained overgrowth was linked with the designed feature size or not. For this purpose, two p-cell structures with wall thicknesses of 120 μm and 150 μm were also printed; thus, the shell thickness is no longer an integer multiple of 50 μm. Interestingly, the overgrowth remains the same, 50 μm, for each free-edge side. Therefore, it is acceptable to justify our result that the overgrowth-induced size error for each free edge is 50 μm. This overgrowth is the key resource for the doubled real density for the studied structures. When the shell thickness was designed to be 100 μm, it is reasonable to obtain a deviation in the density of approximately 100 %. The gyroid structure seems to behave better in the case of the density deviation, which might be linked with its special structural characteristics.

In addition, Fig. 4 and Fig. 5 show that the printed model is not perfect for all curved paths because the local arc is simulated by several square light spots. The designed features in this study were too small for this 50 μm resolution machine to obtain a perfect simulation. This imperfect copy of the smooth TPMS surfaces may lead to some influence on the final mechanical behavior. For future investigations, light scattering-induced overgrowth should be carefully considered when a 3D model is designed.

3.2. Mechanical properties

Samples were tested in a compression test with stress applied parallel to the printing direction, and stress-strain responses were extracted and are presented in Fig. 6. For convenience, the stress-strain responses for

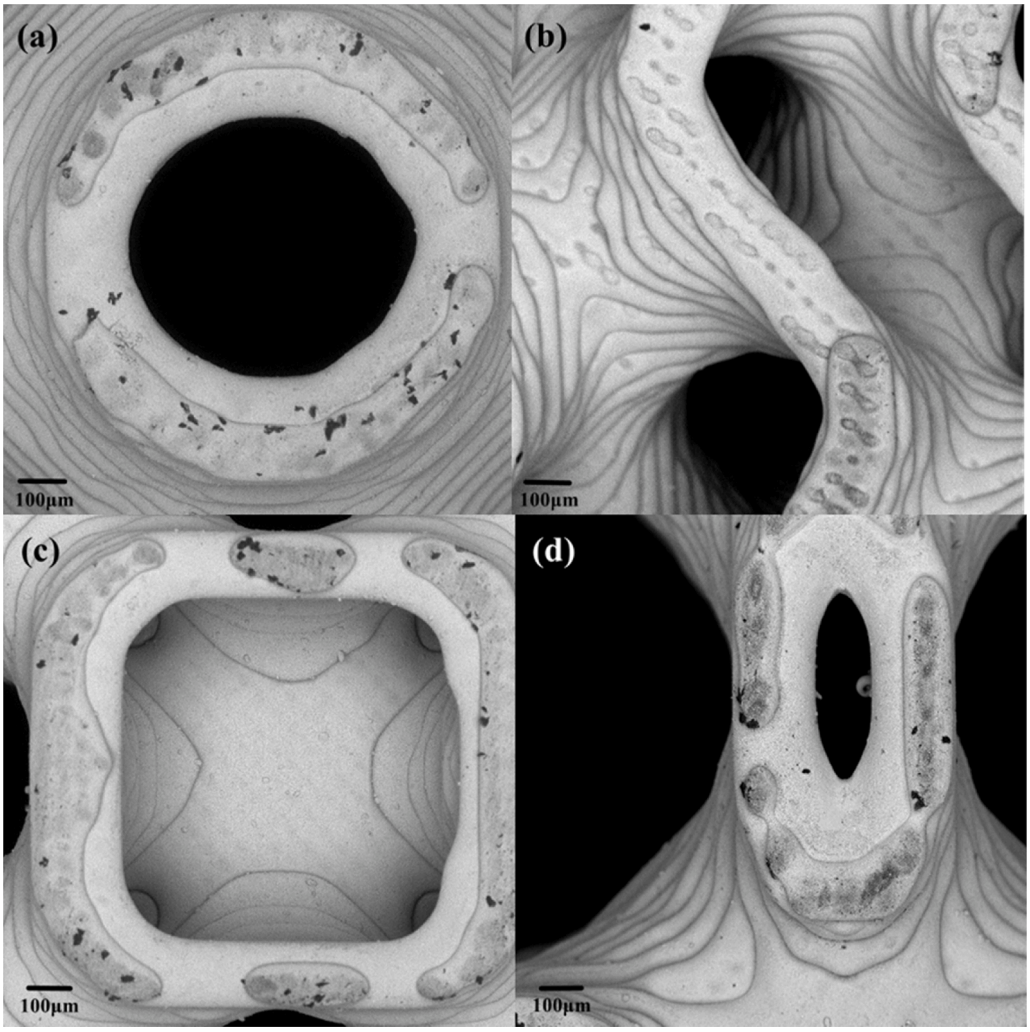

Fig. 4. SEM image of the thickness of all the structures.
(a) p-cell; (b) gyroid; (c) IWP; (d) s14

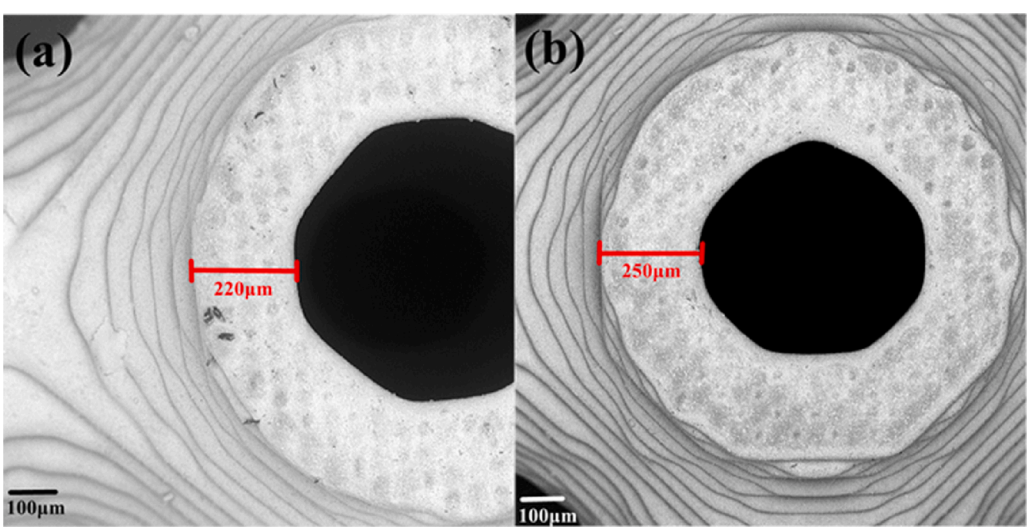

Fig. 5. SEM image of the thickness of the as-printed p-cell structure with shell thicknesses of (a) 120 μm and (b) 150 μm.

the same unit cells with four TPMS structures are presented in the same figure. For the TPMS structures with unit cells less than 3, obvious kinks (Fig. 6 (a) and (b)) can be observed in their stress-strain curves, which may indicate that cracks at local sites might develop without complete catastrophic collapse. When the unit cell number increases to 4 and 5 (Fig. 6 (c) and (d)), the kinks disappear, and only the normal and smooth

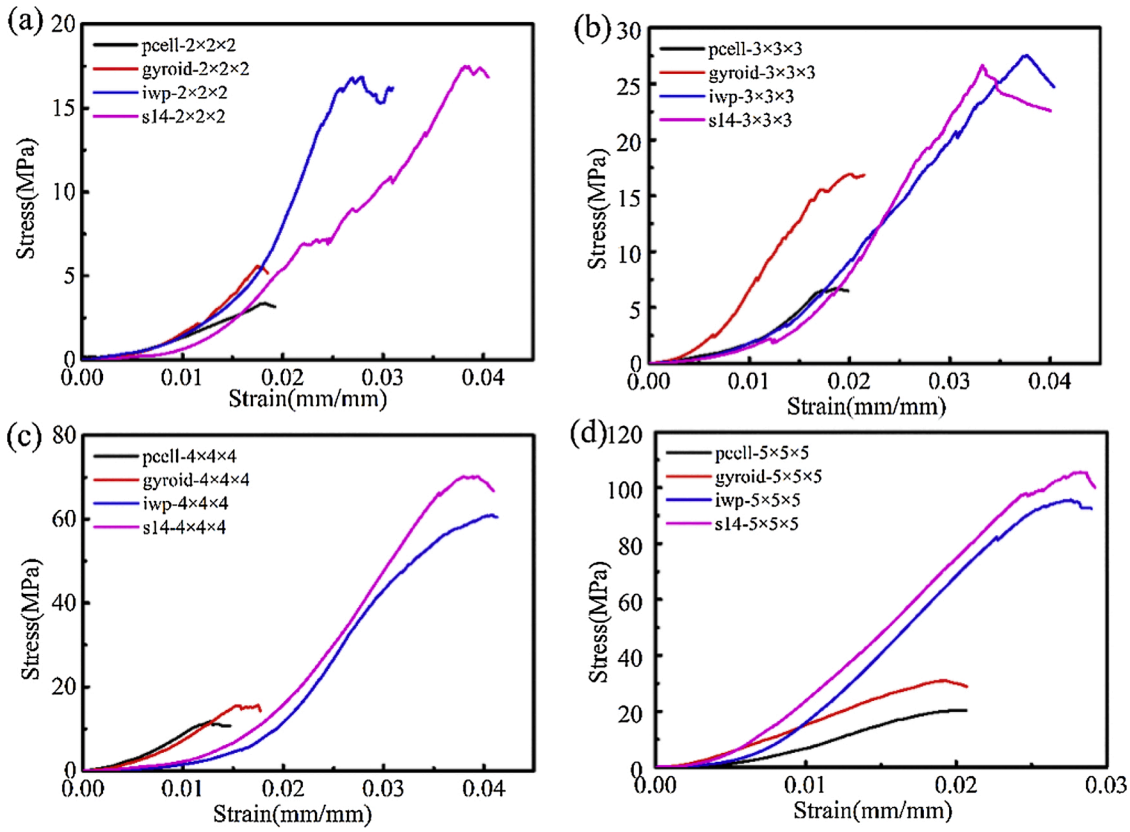

Fig. 6. Stress-strain response of the different TPMS structures prepared in this work.

Table 3
Elastic modulus of four TPMS structures.

TPMS structures		2 × 2×2	3 × 3×3	4 × 4×4	5 × 5×5
	$E_{latt.}$(MPa)	194.7 ± 66.5	800.2 ± 191.4	1312.3 ± 84.5	2006.1 ± 417.3
P-cell	$E_{sol.}$ (GPa)	210	210	210	210
	E^* ($\times 10^{-3}$)	0.9 ± 0.3	3.8 ± 0.9	6.3 ± 0.4	9.6 ± 2.0
	$E_{latt.}$(MPa)	950.1 ± 266.1	1221.2 ± 384.5	1922.4 ± 556.9	2390.5 ± 484.8
Gyroid	$E_{sol.}$ (GPa)	210	210	210	210
	E^* ($\times 10^{-3}$)	4.5 ± 1.3	5.8 ± 1.8	9.2 ± 2.7	11.4 ± 2.3
	$E_{latt.}$ (MPa)	1596.0 ± 245.3	2871.8 ± 54.4	3711.3 ± 289.0	5352.7 ± 232.1
Iwp	$E_{sol.}$ (GPa)	210	210	210	210
	E^* ($\times 10^{-3}$)	7.6 ± 1.2	13.7 ± 0.3	17.7 ± 1.4	25.5 ± 1.11
	$E_{latt.}$ (MPa)	1516.6 ± 359.6	2643.7 ± 185.1	3602.8 ± 429.4	5237.5 ± 719.5
S14	$E_{sol.}$ (GPa)	210	210	210	210
	E^* ($\times 10^{-3}$)	7.2 ± 1.7	12.6 ± 0.9	17.2 ± 2.0	24.9 ± 3.4

Table 4
Compressive strength of four TPMS structures.

TPMS structures		2 × 2×2	3 × 3×3	4 × 4×4	5 × 5×5
	$\delta_{latt.}$(MPa)	3.3 ± 0.5	7.4 ± 1.1	12.2 ± 0.6	20.6 ± 2.3
P-cell	$\delta_{sol.}$ (GPa)	2.5	2.5	2.5	2.5
	δ^* ($\times 10^{-3}$)	1.3 ± 0.2	3.0 ± 0.4	4.9 ± 0.2	8.2 ± 0.9
	$\delta_{latt.}$(MPa)	5.6 ± 1.2	17.0 ± 2.3	22.1 ± 2.5	31.7 ± 3.0
Gyroid	$\delta_{sol.}$ (GPa)	2.5	2.5	2.5	2.5
	δ^* ($\times 10^{-3}$)	2.2 ± 0.5	6.8 ± 0.9	8.8 ± 1.0	12.7 ± 1.2
	$\delta_{latt.}$ (MPa)	18.9 ± 2.7	35.1 ± 2.1	58.2 ± 2.5	96.7 ± 8.0
Iwp	$\delta_{sol.}$ (GPa)	2.5	2.5	2.5	2.5
	δ^* ($\times 10^{-3}$)	6.7 ± 1.2	14.0 ± 0.9	23.3 ± 1.0	38.7 ± 3.2
	$\delta_{latt.}$ (MPa)	17.5 ± 2.4	37.9 ± 2.3	71.6 ± 7.0	104.7 ± 10.5
S14	$\delta_{sol.}$ (GPa)	2.5	2.5	2.5	2.5
	δ^* ($\times 10^{-3}$)	7.0 ± 1.0	15.2 ± 1.0	28.7 ± 2.8	41.9 ± 4.2

Table 5
Physical and mechanical properties for the description of lattices under compression.

Notation	Physical or mechanical property
$\rho_{latt.}$	Density of the structure
$\rho_{sol.}$	Density of the material constituting the lattice
ρ^*	Relative density/volume fraction, equal to $\rho_{latt}/\rho_{sol.}$
Φ	Porosity, equal to 1-ρ^*
$E_{latt.}$	Elastic modulus of the lattice structure
$E_{sol.}$	Elastic modulus of the material constituting the lattice
E^*	Relative elastic modulus of the lattice, equal to $E_{latt}/E_{ol.}$
$\delta_{latt.}$	Compressive strength of the lattice structure
δ_{sol}	Yield strength of the material constituting the lattice
δ^*	Relative strength of the lattice, equal to $\delta_{latt}/\delta_{sol.}$

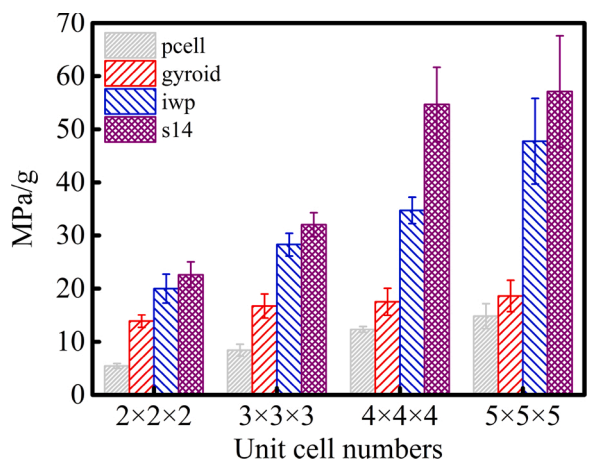

Fig. 7. Bar graph of the specific compressive strength of different TPMS structures.

increase in stress over the strain can be observed. In addition, two distinct compressive strain thresholds can be noticed for these 4 TPMS structures. P-cells and gyroids exhibited similar maximum strains of approximately 0.015−0.02, while IWPs and s14 s presented higher maximum strains of approximately 0.03−0.04. It should be noted that a structure built through a layer-by-layer mode could still have some structural defects at the interlayer boundaries or inside the layers. Therefore, the dispersion in the maximum strain should be regarded as reasonable. It is clear that IWPs and s14 s presented clear advantages over p-cells and gyroids in terms of either compressive strength or maximum strain.

From the stress-strain curves, different mechanical properties were deduced. Young's modulus (compression) is determined by the slope of the curve for the elastic region. Young's modulus may be characterized as the stiffness or the ability of the structure to resist deformation within the linear portion. We obtained the elastic modulus of the TPMS structure from the slope of the straight part of the stress-strain curve of each model. In fact, the stress-strain curve is not strictly linear due to the possible invisible cracks in the sample, so there is a certain error in determining the straight part. Fracture strength is the highest stress in the stress-strain curve and it is defined as the stress at which specimens fail via fracture. On count of this, the elastic modulus (Table 3) and compressive strength (Table 4) were averaged from at least 5 samples, and the relevant physical properties are given in Table 5.

To further discuss the difference between the 4 TPMS structures, we calculated the specific compressive strength, and the results are presented in Fig. 7. Regardless of the unit cell numbers in the structures, the specific compressive strength followed the order of s14 > IWP > gyroid > p-cell. Here, the potential influence of the real density had already been excluded; thus, the structural characteristics from the TPMS structures truly showed a strong effect on the compressive

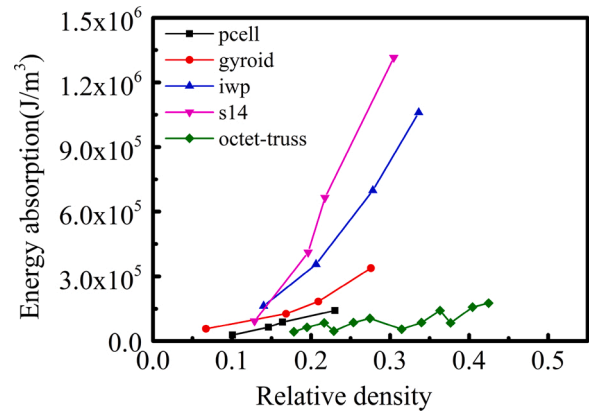

Fig. 8. Energy absorption of four TPMS structures and octet-truss with the variation of the relative density.

strength. Among all four TPMSs, the gyroid structure showed a rather stable performance in the specific strength when the cell number/relative density was changed. This might indicate that gyroid might be less sensitive to structural defects. However, for general engineering applications, IWP and s14 should be highly because of their higher strength. Deviations in density are inevitable for photopolymerization-based 3D ceramic printing technology, so it will be interesting to further study the differences between IWP and s14 when the cell numbers can be increased further.

Fig. 8 shows the variation of the energy absorption for all the prepared TPMS structures with changing real relative density. Different from lightweight metal structures, where substantially large deformation and densification can always be found, lightweight ceramic structures were still brittle, and the strain was at least one order of magnitude than in their metal counterparts. Even so, IWP and s14 zirconia structures can reach an absorption energy of $>10^6$ J/m^3, which is close to the bottom range for metal TPMS structures [27]. Similar to the compressive strength, IWPs and s14 s also demonstrated their superiority over p-cells and gyroids in energy absorption. However, all the TPMS structures presented better performance in energy absorption than the classic octet-truss structure if a similar density range was considered. It is rational to conclude that TPMSs generally presented better mechanical properties than classic lattice structures such as octet-truss. In this respect, the results for ceramic materials are consistent with those obtained for metal mechanical metamaterials [17].

Notably, the four different TPMS structures presented quite different slopes for the increase in absorption energy with the increase in relative density. The s14 and IWP structures showed much higher sensitivity of energy absorption to changes in structural density. They can be regarded as more efficient at reaching the target for lightweight design. The IWP and s14 structures should have advantages when the specific strength and mechanical load were selected to be the design priority without strict limits on the density. However, we cannot neglect the superiority of the gyroid structure when low density, especially <10 %, is the primary requirement for the application in mind.

In general, for highly porous cellular materials, often called "foams", there is a strong tradition, going back to the classical work of Gibson and Ashby [20] of understanding their effective properties in terms of power-law relations [25]. The following are the Eqs. (3,4) for the relations between the elastic modulus and relative density and compressive strength and relative density:

$$\frac{E_{latt.}}{E_{sol.}} = C_1\left(\frac{\rho_{latt.}}{\rho_{sol.}}\right)^n. \quad (3)$$

$$\frac{\delta_{latt.}}{\delta_{sol.}} = C_2\left(\frac{\rho_{latt.}}{\rho_{sol.}}\right)^m. \quad (4)$$

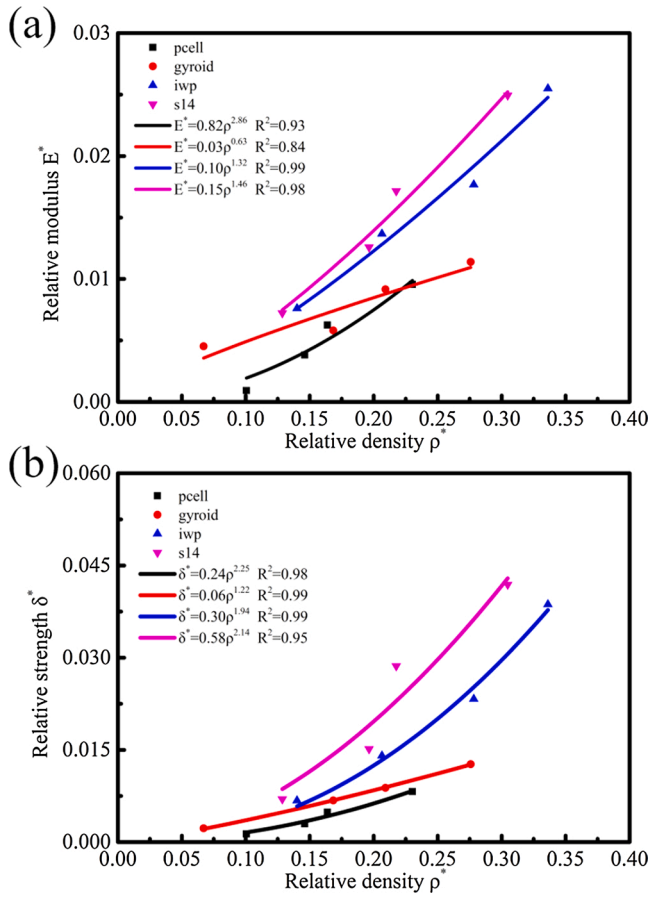

Fig. 9. Variation of (a) the relative modulus and (b) relative strength of the zirconia TPMS structures with relative density [20].

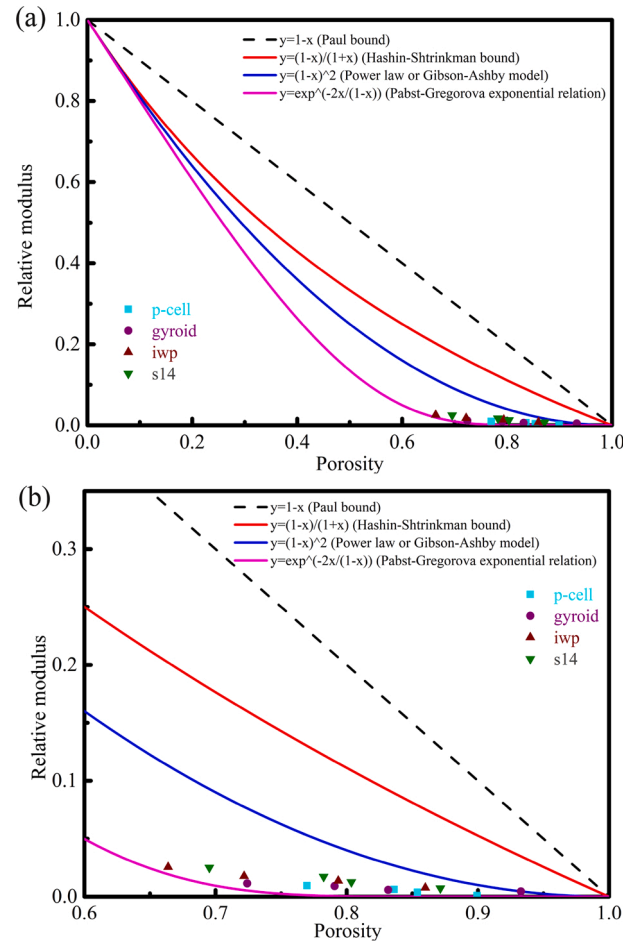

Fig. 10. a) Comparison of relative elastic modulus values of different TPMS structures with the upper Paul bound (black dash line), the upper Hashin-Shtrikman bound (red line), the power-law prediction (also called Gibson-Ashby relation, blue line) and the (Pabst-Gregorová) exponential prediction (purple curve) (For interpretation of the references to colour in this figure legend, the reader is referred to the web version of this article).

The pre-factors C_1 and C_2 can be considered as control parameters for the GA model. In particular, for Young's modulus C_1 should be close to unity (theoretically exactly 1) for the GA model to be adequate. The values of C_1, C_2, n and m can be determined by fitting existing or measured data, but n and m depend on the geometry and, in particular, the deformation mechanisms of the cells in question and should not exceed certain limits, otherwise the GA model is inadequate. A scaling exponent n close to 1 indicates that the structures exhibited a stretch-dominated deformation behavior, whereas an exponent of 2 typically indicates a bending-dominated deformation [29].

Here, we analysed the relative elastic modulus and relative strength over the density to justify the difference between the TPMS structures we studied (see Fig. 9). Even with the limited data—only 4 data points for each TPMS structure—we can see the distinct difference between TPMS structures in either relative modulus or relative strength. For the curve fitting, we used 210 GPa and 2.5 GPa [30] as the elastic modulus and compressive strength for the solid zirconia ceramic. To avoid misinterpretation and confusion, we drew the graph as a power function and our fitting software is excel and Origin.

Fig. 9(a) shows that the pre-factor values (C_1) range from 0.03 to 0.15 (except p-cell), which is a clear indication that the GA model is not an appropriate theoretical setting for interpreting the data measured here, because it has to be emphasized that the pre-factor is a control parameter. When its value far off unity (i.e. far away from 1) the GA model cannot be used.

(b) Enlarged view of porosity and relative modulus

The relative elastic modulus of porous materials is bounded from above by the upper Paul bound [31]:

$$E^* = 1 - \Phi \tag{5}$$

This upper bound can be realized only for property values in the axial direction of translationally invariant, i.e. extremely anisotropic microstructures.

For isotropic porous materials, the relative elastic modulus is bounded by the upper Hashin-Shtrikman bounds [32]:

$$E^* = \frac{1-\Phi}{1+\Phi} \tag{6}$$

Many real porous materials, are known to obey approximately either the power-law relations (GA model) [20]:

$$E^* = (1-\Phi)^2 \tag{7}$$

or the (Pabst-Gregorová) exponential relations [33]:

$$E^* = e^{\left(\frac{-2\Phi}{1-\Phi}\right)} \tag{8}$$

To study the relationship between relative density (porosity) and relative modulus, we draw on the conclusion of Pabst et al. [25]. It can be seen from Fig. 10(a) that the elastic modulus (as determined from compression tests) of ceramic TPMS structures is much lower than predicted by the GA model and much closer to the PG exponential prediction. In order to see this more clearly, we enlarged the part of interest to get Fig. 10(b). It can be clearly seen that the elastic modulus of most ceramic TPMS structures is still slightly higher than predicted by the PG exponential relation. It is worth nothing that the gyroid

structures conforms to the prediction of the GA model at the porosity of 93.3 %. In general, the effective properties of 3D printed ceramic TPMS structures prepared in this work are in relatively good agreement with the PG exponential prediction. The TPMS structures were also defined as one kind of shelluar structures, which potentially introduce some deviation from the typical open cell structures. In brief, further efforts are needed for a full understanding of the effective property models for novel ceramic structures prepared by 3D printing.

4. Conclusions

Four ceramic TPMS structures based on a mathematical surface were successfully fabricated by the DLP technique, and their mechanical properties were experimentally determined. The relative density was adjusted by changing the cell numbers. The order of compressive strength was s14>IWP>gyroid>p-cell. The ceramic TPMS structure allowed at least 2% deformation. At a low relative density (6.7 %), a compressive strength of 5.6 MPa can be reached for the gyroid structure, which has potential for practical lightweight application. At a relative density of 30.5 %, the s14 structure has a reasonably good compressive strength of 105 MPa. The relationship between Young's modulus and porosity of zirconia TPMS structures obey the PG exponential prediction with better precision than the classical GA model.

Declaration of Competing Interest

The authors declare that they have no known competing financial interests or personal relationships that could have appeared to influence the work reported in this paper.

Acknowledgements

The authors highly acknowledge the financial support of the National Key R&D Program of China (No.2017YFB1103500 & No.2017YFB1103502). The findings, conclusions, and recommendations expressed in this manuscript are those of the authors and do not necessarily reflect the views of the NKPC.

References

[1] D.W. Abueidda, I. Jasiuk, N.A. Sobh, Acoustic band gaps and elastic stiffness of PMMA cellular solids based on triply periodic minimal surfaces, Mater. Des. 145 (2018) 20–27.
[2] D.W. Abueidda, R.K. Abu Al-Rub, A.S. Dalaq, H.A. Younes, A.A. Al Ghaferi, T. K. Shah, Electrical conductivity of 3D periodic architectured interpenetrating phase composites with carbon nanostructured-epoxy reinforcements, Compos. Sci. Technol. 118 (2015) 127–134.
[3] L. Peisheng, Q. Haibing, H. Hongliang, W. Yaoqi, Z. Yanling, EMI shielding and thermal conductivity of a high porosity reticular titanium foam, Mater. Des. 92 (2016) 823–828.
[4] L. Min Geun, L. Jeong Woo, H. Seung Chul, K. Kiju, Mechanical analyses of "Shellular", an ultralow-density material, Acta Mater. 103 (2016) 595–607.
[5] A. Vigliotti, V.S. Deshpande, D. Pasini, Non linear constitutive models for lattice materials, J. Mech. Phys. Solids 64 (2014) 44–60.
[6] D.W. Abueidda, R.K. Abu Al-Rub, A.S. Dalaq, D.-W. Lee, K.A. Khan, I. Jasiuk, Effective conductivities and elastic moduli of novel foams with triply periodic minimal surfaces, Mech. Mater. 95 (2016) 102–115.
[7] Y. Dongjin, Porous scaffold design using the distance field and triply periodic minimal surface models, Biomaterials. 32 (2011) 7741–7754.
[8] Y. Dongjin, K.-H. Kim, An advanced multi-morphology porous scaffold design method using volumetric distance field and beta growth function, Int. J. Precis. Eng. Manuf. 16 (2015) 2021–2032.
[9] Y. Dongjin, New paradigms in hierarchical porous scaffold design for tissue engineering, Mater. Sci. Eng. C 33 (2013) 1759–1772.
[10] Y. Dongjin, New paradigms in cellular material design and fabrication, Int. J. Precis. Eng. Manuf. 16 (2015) 2577–2589.
[11] Y. Dongjin, Recent trends and challenges in computer-aided design of additive manufacturing-based biomimetic scaffolds and bioartificial organs, Int. J. Precis. Eng. Manuf. 15 (2014) 2205–2217.
[12] M. Hofmann, 3D printing gets a boost and opportunities with polymer materials, ACS Macro Lett. 3 (2014) 382–386.
[13] R.D. Goodridge, C.J. Tuck, R.J.M. Hague, Laser sintering of polyamides and other polymers, Prog. Mater. Sci. 57 (2012) 229–267.
[14] D.W. Abueidda, M. Bakir, R.K. Abu Al-Rub, J.S. Bergström, N.A. Sobh, I. Jasiuk, Mechanical properties of 3D printed polymeric cellular materials with triply periodic minimal surface architectures, Mater. Des. 122 (2017) 255–267.
[15] D.W. Abueidda, M. Elhebeary, C.-S. Shiang, S. Pang, R.K. Abu Al-Rub, I.M. Jasiuk, Mechanical properties of 3D printed polymeric Gyroid cellular structures: experimental and finite element study, Mater. Des. 165 (2019) 107597.
[16] I. Maskery, L. Sturm, A.O. Aremu, A. Panesar, C.B. Williams, C.J. Tuck, R. D. Wildman, I.A. Ashcroft, R.J.M. Hague, Insights into the mechanical properties of several triply periodic minimal surface lattice structures made by polymer additive manufacturing, Polymer. 152 (2018) 62–71.
[17] O. Al-Ketan, R. Rowshan, R.K. Abu Al-Rub, Topology-mechanical property relationship of 3D printed strut, skeletal, and sheet based periodic metallic cellular materials, Addit. Manuf. 19 (2018) 167–183.
[18] I. Maskery, N.T. Aboulkhair, A.O. Aremu, C.J. Tuck, I.A. Ashcroft, Compressive failure modes and energy absorption in additively manufactured double gyroid lattices, Addit. Manuf. 16 (2017) 24–29.
[19] H. Seung Chul, L. Jeong Woo, K. Kiju, A new type of low density material: shellular, Adv. Mater. 27 (2015) 5506–5511.
[20] M.F. Ashby, The properties of foams and lattices, Philos. Trans. Math. Phys. Eng. Sci. 364 (2006) 15–30.
[21] Z. Lei, F. Stefanie, D. Stephen, C. Shuai, Y.W. Michael, W. Jun, F.L. Wen, Pseudo-ductile fracture of 3D printed alumina triply periodic minimal surface structure, J. Eur. Ceram. Soc. 40 (2020) 408–416.
[22] M.P. Oraib Al-Ketan, Alberto Ortona, Rashid K. Abu Al-Rub, Additive manufacturing of architected catalytic ceramic substrates based on triply periodic minimal surfaces, J. Am. Ceram. Soc. 102 (2019) 6176–6193.
[23] S. Minhao, W. Cao, Z. Zhe, Mechanical properties of ZrO_2 TPMS structures prepared by DLP 3D printing, in: IOP Conference Series: Materials Science and Engineering, 678, 2019, p. 012017.
[24] W. Pabst, E. Gregorová, G. Tichá, Elasticity of porous ceramics—a critical study of modulus−porosity relations, J. Eur. Ceram. Soc. 26 (2006) 1085–1097.
[25] W. Pabst, T. Uhlířová, E. Gregorová, A. Wiegmann, Young's modulus and thermal conductivity of closed-cell, open-cell and inverse ceramic foams – model-based predictions, cross-property predictions and numerical calculations, J. Eur. Ceram. Soc. 38 (2018) 2570–2578.
[26] T. Uhlířová, W. Pabst, Conductivity and Young's modulus of porous metamaterials based on Gibson-Ashby cells, Scr. Mater. 159 (2019) 1–4.
[27] Z. Lei, F. Stefanie, D. Stephen, C. Shuai, Y.W. Michael, W. Jun, et al., Energy absorption characteristics of metallic triply periodic minimal surface sheet structures under compressive loading, Addit. Manuf. 23 (2018) 505–515.
[28] G. Mitteramskogler, R. Gmeiner, R. Felzmann, S. Gruber, C. Hofstetter, J. Stampfl, et al., Light curing strategies for lithography-based additive manufacturing of customized ceramics, Addit. Manuf. 1-4 (2014) 110–118.
[29] W. Lifeng, L. Jacky, E.L. Thomas, M.C. Boyce, Co-continuous composite materials for stiffness, strength, and energy dissipation, Adv. Mater. 23 (2011) 1524–1529.
[30] D. Fabris, J. Mesquita-Guimarães, P. Pinto, J.C.M. Souza, M.C. Fredel, F.S. Silva, et al., Mechanical properties of zirconia periodic open cellular structures, Ceram. Int. 45 (2019) 15799–15806.
[31] B. Paul, Prediction of elastic constants of multiphase materials, Transactions of the Metallurgical Society. 218 (1960) 36–41.
[32] Z. Hashin, S. Shtrikman, A variational approach to the theory of the effective magnetic permeability of multiphase materials, J. Appl. Phys. 33 (1963) 3125–3131.
[33] W. Pabst, E. Gregorová, M. Černý, Isothermal and adiabatic Young's moduli of alumina and zirconia ceramics at elevated temperatures, J. Eur. Ceram. Soc. 33 (2013) 3085–3093.